

RESEARCH LETTER

10.1002/2017GL073203

Key Points:

- Intermodel diversity in ENSO variability is mainly attributed to that in thermocline feedback
- Intermodel thermocline feedback is highly correlated to the intermodel sensitivity of the zonal contrast of thermocline to wind stress
- Oceanic response is related to the intermodel diversity in the wind stress curl response to SST

Supporting Information:

- Supporting Information S1

Correspondence to:

S.-I. An,
sian@yonsei.ac.kr

Citation:

An, S.-I., E. S. Heo, and S. T. Kim (2017), Feedback process responsible for intermodel diversity of ENSO variability, *Geophys. Res. Lett.*, *44*, 4272–4279, doi:10.1002/2017GL073203.

Received 22 FEB 2017

Accepted 24 APR 2017

Accepted article online 26 APR 2017

Published online 13 MAY 2017

Feedback process responsible for intermodel diversity of ENSO variability

Soon-Il An¹ , Eun Sook Heo¹ , and Seon Tae Kim² 
¹Department of Atmospheric Sciences, Yonsei University, Seoul, South Korea, ²Climate Prediction Department, APEC Climate Center, Busan, South Korea

Abstract The origin of the intermodel diversity of the El Niño–Southern Oscillation (ENSO) variability is investigated by applying a singular value decomposition (SVD) analysis between the intermodel tropical Pacific sea surface temperature anomalies (SSTA) variance and the intermodel ENSO stability index (BJ index). The first SVD mode features an ENSO-like pattern for the intermodel SSTA variance (74% of total variance) and the dominant thermocline feedback (TH) for the BJ index (51%). Intermodel TH is mainly modified by the intermodel sensitivity of the zonal thermocline gradient response to zonal winds over the equatorial Pacific (β_h), and the intermodel β_h is correlated higher with the intermodel off-equatorial wind stress curl anomalies than the equatorial zonal wind stress anomalies. Finally, the intermodel off-equatorial wind stress curl is associated with the meridional shape and intensity of ENSO-related wind patterns, which may cause a model-to-model difference in ENSO variability by influencing the off-equatorial oceanic Rossby wave response.

1. Introduction

El Niño and its opposite phase, the La Niña (together El Niño–Southern Oscillation: ENSO), are anomalous year-to-year sea surface warming and cooling events, respectively, over the tropical central-to-eastern Pacific. Such interannual fluctuations of tropical Pacific sea surface temperature (SST) cause severe climatic and socioeconomic damages over almost all parts of the Earth [McPhaden, 2003]. Therefore, the accurate forecast of ENSO obviously provides a great benefit to people. Not only the short-term forecasts but also the future climate projections of ENSO have been drawing great attention [Collins et al., 2010; Cai et al., 2015]. Despite significant improvements in representing ENSO in climate models [Bellenger et al., 2014], uncertainties in the future projection and seasonal forecast of ENSO due to various model errors still remain [Christensen et al., 2013].

In order to reduce the model bias for ENSO, better simulation of tropical climate states is required because of a rigid dynamical connection between the mean climate state and ENSO variability [e.g., An and Wang, 2000; Guilyardi, 2006; Jin et al., 2008; Yeh et al., 2014; Ham and Kug, 2015]. Most common mean biases over the tropical Pacific in climate models are too intense and too far westward location of the equatorial cold tongue, a narrow meridional width of SST anomaly pattern [Li and Xie, 2012], a westward shift of climatological precipitation patterns over the equatorial Pacific [Ham and Kug, 2015], and the double Intertropical Convergence Zone in the eastern Pacific [Lin, 2007; Oueslati and Bellon, 2015]. Obviously, those mean biases are dynamically connected to the bias of ENSO variability. In this regard, a flux correction to reduce such mean biases improves the representation of ENSO including the ENSO variability [Magnusson et al., 2013], and a statistical correction of the mean precipitation pattern also improves ENSO-induced precipitation in the multimodel ensemble (MME) [Ham and Kug, 2015].

As we mentioned above, to unveil the origin of ENSO bias in climate models is quite a challenging problem because mean state bias and variability bias have to be dealt with simultaneously. Thus, most studies have focused on revealing how the mean state is responsible for the variability bias. Meanwhile, process-oriented ENSO metrics were proposed as a method to evaluate the simulated ENSO by various climate models and to provide great insights on the internal feedback process causing ENSO bias [Bellenger et al., 2014]. However, no study has yet performed a systematic analysis to objectively quantify the relationship between ENSO amplitude bias and the air-sea coupled feedback for ENSO. Here using singular value decomposition (SVD) analysis [Wallace et al., 1992] (i.e., maximum covariance method), we objectively and quantitatively identify the relationship between the intermodel diversity/bias in ENSO

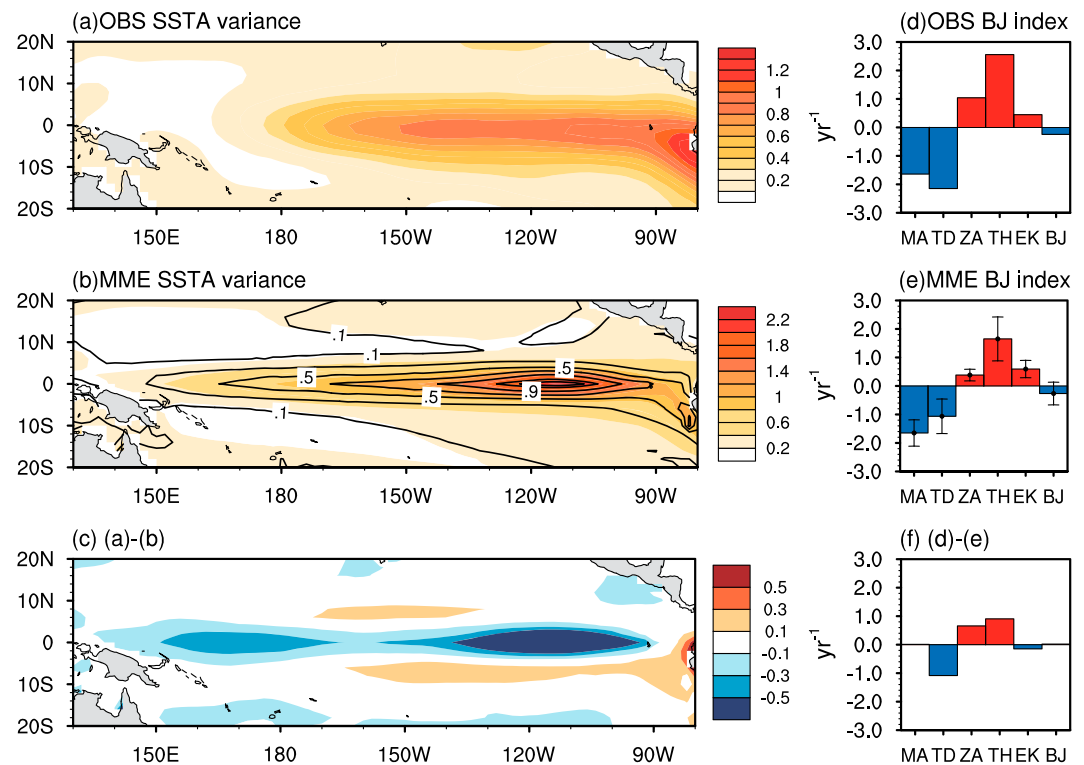


Figure 1. (a) Variance of observed tropical Pacific sea surface temperature (SST) anomalies. (b) Multimodel ensemble mean of tropical Pacific SSTA variance (shading) and intermodel standard deviation of SSTA variance (contour with 0.2 intervals). (c) Difference between the observed SSTA variance and MME of model SSTA variance. (d) BJ index from the observation and SODA data (red bar for positive and blue bar for negative values). (e) As in Figure 1d but for multimodel ensemble mean of BJ index obtained from 21 CMIP5 models. Whisker indicates the range of one standard deviation of the BJ index of each model. (f) Difference in the BJ index between the observation based and MME. Units for shading and contours in Figures 1a–1c are °C² and °C, respectively. Units for the bars in Figures 1d–1f are year^{−1}.

variability and feedback processes in climate models participating in the Coupled Model Intercomparison Project Phase 5 (CMIP5), and our results highlight the most involved physical processes. Section 2 introduces the data and the models utilized. The main results and summary/discussion are presented in sections 3 and 4, respectively.

2. Data and Method

2.1. Observed Data and Model Outputs

In this study, observed monthly SST derived from the National Oceanic and Atmospheric Administration Extended Reconstructed SST (ERSST) version 4 [Huang *et al.*, 2014] and ocean temperature derived from the Simple Ocean Data Assimilation (SODA) version 2.2.4 [Carton and Giese, 2008] spanning from 1951 to 2000 are utilized. SODA was used for Bjerknes stability index (BJ index) computation shown in Figure 1d. Anomalies are computed by removing the monthly mean climatological annual cycle for the whole period of each data set, and linear trends are removed.

The twentieth century simulation (i.e., “historical” runs) forced by the observed atmospheric composition changes and time-evolving land cover are obtained from 21 CMIP5 coupled general circulation models (CGCM) [Taylor *et al.*, 2012]. Because of the limited availability of ocean subsurface data, only 21 CGCMs, which are listed in Table S1 in the supporting information, are utilized. Descriptions of individual models can be found at <http://www-pcmdi.llnl.gov/>. Finally, computation of the BJ index had been done for 1951–2000 for the observation/SODA and 21 CGCMs [Kim *et al.*, 2014].

2.2. BJ Index

Jin *et al.* [2006] introduced a method to compute the linear growth rate of ENSO based on a two-box approximation of a simplified prototype ENSO model, the so-called “recharge oscillator.” This Bjerknes stability index (BJ index) analysis classifies the positive and negative feedback dynamics. Here a two-box simplification of the recharge oscillator representing western and eastern tropical Pacific within 5°S–5°N is originated from the partial flux form of an SST equation [Kang *et al.*, 2001]. Ensemble dynamics, referring that the dynamical/physical parameters identifying ENSO characteristics have been statistically quantified from data, are proposed for the linear growth rate, R [Jin *et al.*, 2006]. The total BJ index, BJ (i.e., growth rate), is defined as

$$2BJ + \varepsilon = - \left[a_1 \frac{\langle \Delta \bar{u} \rangle_E}{L_x} + a_2 \frac{\langle \Delta \bar{v} \rangle_E}{L_y} \right] - \alpha_s + \mu_a \beta_u \left\langle -\frac{\partial \bar{T}}{\partial x} \right\rangle_E + \mu_a \beta_h \left\langle \frac{\bar{w}}{H_1} \right\rangle_E a_h + \mu_a \beta_w \left\langle -\frac{\partial \bar{T}}{\partial z} \right\rangle_E, \quad (1)$$

where ε corresponds to the rate that the ocean adjusts to damping processes [Kim and Jin, 2011], and again, BJ becomes the linear growth rate of an oscillatory system [Jin *et al.*, 2006]. Each feedback term and associated response sensitivity coefficients are documented in Table S3. Therefore, when $BJ > 0$, the ENSO system is linearly unstable, otherwise stable. The details of terms and the driving equation appear in Jin *et al.* [2006] and Kim and Jin [2011]. The node between the western and eastern boxes was determined by computing the regression map of the ocean heat content anomalies against the normalized principal component time series of the first empirical orthogonal function mode of the anomalous SST following the method of Kim and Jin [2011]. The first two terms on the right side of equation (1) represent damping by the thermal advection by mean currents (MA) and comprehensive thermodynamic damping (TD), respectively; the last three terms represent growth by zonal advection feedback (ZA), thermocline feedback (TH), and Ekman feedback (EK), respectively. All parameter values of the BJ index utilized in this study are the same as those used in Kim *et al.* [2014].

3. Results

The existence of intermodel diversity might be obvious because each model’s structure, including the dynamic core and physical parameterization, is different. However, since a numerical model has been developed based on the physical and dynamical laws of nature, it is supposed to simulate nature realistically. Therefore, the intermodel diversity in ENSO must be due to inadequate or insufficient model physics. While some may argue that the intermodel ENSO diversity is also expected because of a diversity/complexity nature of ENSO [Capotondi *et al.*, 2015], even the historical runs from most of CMIP5 models are suffered by a deficiency in simulating the observed diversity of ENSO [e.g., Xu *et al.*, 2017], implying that the intermodel diversity in ENSO is mainly due to the problem of a model itself.

Here we compute MMEs of the mean and standard deviation of tropical Pacific SSTA variance (Figure 1). A larger standard deviation indicates larger intermodel diversity in ENSO variability. As shown in Figures 1a and 1b, the overall pattern of variance of SST anomalies obtained from 21 CMIP5 models is similar to the observed data. However, while the MME overestimates ENSO variability over the equatorial region, it slightly underestimates it over the off-equatorial region (Figure 1c), meaning that ENSO variability in models is relatively more confined to the equator compared to the observation data. Furthermore, the range of one standard deviation is relatively large (~ 1.0) over the equatorial eastern Pacific, indicating that strong intermodel diversity exists, and the intermodel diversity is directly linked to the model bias in ENSO variability.

The BJ index and linear feedback terms in equation (1) obtained from the observation/SODA (hereafter “observation based”) show that MA (-1.64) and TD (-2.15) are negative (damping process), and ZA (1.05), TH (2.56), and EK (0.45) are positive (growing process); the BJ index is -0.25 year^{-1} (Figure 1d) [Kim and Jin, 2011], indicating that the observed ENSO is likely a damped oscillator. The MME of the BJ index obtained from 21 CMIP5 models is similar to the observation-based BJ index, but each linear feedback term is somewhat different compared to the observation-based one (Figure 1f). The negative feedback by TD and the positive feedbacks by both ZA and TH obtained from the 21 models are smaller than those obtained from the observation-based data. Consequently, the compensation between two opposite biases results in an apparently correct value of the BJ index. As can be seen in Figure 1e, the ranges of one standard deviation of the intermodel BJ index including each linear feedback term are rather wide.

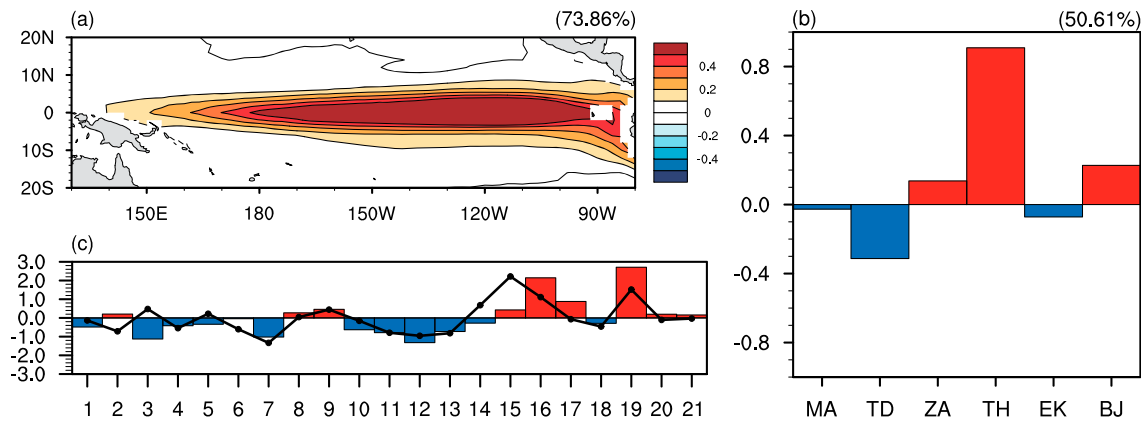


Figure 2. First SVD mode of (a) the intermodel tropical Pacific SSTA variance and (b) intermodel BJ index obtained from 21 CMIP5 models and (c) corresponding principal components (PCs). Percentages of explained variance are represented in the upper right corner of each panel. In Figure 2c, the bars and line indicate PCs for SSTA variance and BJ index, respectively, and the numbers along the x axis indicate each model. Variance explained by the first SVD mode is 92.6% of the total variance. The correlation between two PCs is 0.65 (significant at 99% confidence level). Numbers in Figure 2c represent each model listed in Table S1.

To objectively quantify the relationship between the amplitude of ENSO and feedback processes in the intermodel diversity of the 21 CMIP5 models, we obtain the SVD mode between the intermodel tropical Pacific SSTA variance and the intermodel BJ index (including five linear feedback components). Therefore, the leading SVD mode represents the most coherent pattern between the intermodel diversity of ENSO variability and that of ENSO-related feedback intensity. The first and second SVD modes explain 92.6% (73.9% for total variance of intermodel SSTA variance and 50.6% for total variance of intermodel BJ index) and 5.1% (4.4% for total variance of SSTA variance and 27.3% for total variance of BJ index) of total coupled variance, respectively (Figure 2; the second SVD mode is not shown). Because of the small variance explanation of the second SVD mode of intermodel SSTA variance, in this study we mainly focus on the first SVD mode. The correlation coefficient between two principal components (PCs) is 0.65, which is statistically significant over the 99% confidence level. Here a null hypothesis (i.e., “uncorrelated” so $\rho = 0.0$) is tested by a Student’s *t* test.

As shown in Figure 2, the first SVD mode pattern for the intermodel SSTA variance is summarized as an equatorially confined and zonally elongated shape with its maximum loading over the central-to-eastern Pacific, which resembles a typical El Niño SSTA pattern or the MME of the tropical Pacific SSTA variance (see Figure 1b). Therefore, the first SVD mode represents the overestimation or underestimation of ENSO variability among 21 models. The first SVD mode of the BJ index (and feedback terms) features a dominant TH and slightly enhanced TD, and all together a slightly enhanced BJ index. A positive BJ index is dynamically consistent with the larger SSTA variance in comparison to the MME and the observation-based results. Similarly, *Chen et al.* [2015] mentioned that the distinct model-to-model ENSO amplitude response in future global warming scenarios among four coupled GCMs is attributed to TH and ZA. In summary, the intermodel diversity in ENSO amplitude is closely related to the intermodel diversity of TH. Moreover, a correlation between the intermodel Niño-3.4 standard deviation and the intermodel TH is 0.69, which is statistically significant over 99% confidence level.

Here we focus on the intermodel TH to determine what process is primarily responsible for the intermodel diversity of TH. As we have seen in equation (1), $TH (= \mu_a \beta_h \left\langle \frac{\bar{w}}{H_1} \right\rangle_E a_h)$ is a combination of four components:

1. μ_a : Sensitivity of the surface wind response to SST forcing represented by $[\tau_x] = \mu_a \langle T \rangle_E$, where $[\tau_x]$ is the equatorial basin-wide (121°E–82°W) zonal wind stress anomaly, and $\langle T \rangle_E$ is the SST anomaly over the equatorial eastern Pacific ($\rho = 0.66^{**}$);
2. β_h : Sensitivity of the zonal tilt of the equatorial thermocline depth between the eastern and western Pacific with respect to zonal wind stress forcing obtained by using $\langle h \rangle_E - \langle h \rangle_W = \beta_h [\tau_x]$, where $\langle h \rangle_E$ and $\langle h \rangle_W$ are the thermocline depth anomalies over eastern and western Pacific, respectively ($\rho = 0.91^{**}$);
3. a_h : Sensitivity of the ocean subsurface temperature anomaly with respect to the thermocline depth change represented by $\langle H(\bar{w}) T_{sub} \rangle_E = a_h \langle h \rangle_E$, where $H(\bar{w})$ is a Heaviside function depending on the

mean upwelling and T_{sub} is the subsurface temperature anomaly below the mixed layer over the equatorial eastern Pacific ($\rho = 0.14$);

4. $\left\langle \frac{\bar{w}}{H_1} \right\rangle_E$: Mean upwelling velocity at the mixed layer over the equatorial eastern Pacific, where H_1 is a constant mixed layer depth of 50 m ($\rho = 0.00$).

To determine the most related component, we calculate the correlation coefficient between TH and the above four components of each model (see coefficients in the bracket above or Table S2). The correlation between above four components and the first SVD PCs of the BJ index produced a similar result (see Table S2). The correlations of TH with μ_a and β_h are statistically significant with the 99% confidence (marked by **), indicating that the intermodel diversity of TH is mainly attributed to the intermodel diversities of β_h and μ_a . In other words, the intermodel diversity in ENSO variability featuring an ENSO-like pattern is mainly related to the intermodel diversity in the sensitivity of the ocean dynamics response to wind stress and the sensitivity of the wind response to ENSO-related SST anomalies. Similarly, *Borlace et al.* [2013] mentioned that the multidecadal modulation of ENSO amplitude that appears in a 1000 year simulation of a coupled model is mainly governed by changes in β_h .

We now proceed one step further to determine what drives the intermodel diversity of β_h . The β_h is basically affected by two factors: ocean stratification and wind stress pattern/intensity (i.e., its zonal and meridional shape) [e.g., *An and Kang*, 2001; *Chen et al.*, 2015; *Im et al.*, 2015; *An and Kim*, 2017]. Therefore, the intermodel β_h and μ_a are dynamically linked (see also section 4).

Under a simple dynamical framework, we have $\beta_h \approx \frac{L}{2\rho_o g' H}$ [*Hirst*, 1986; *An and Kang*, 2001; *An and Bong*, 2016], where L is the ocean basin length, H is the mean thermocline depth, ρ_o is the ocean water density, and g' is the reduced gravity. An inverse relationship between β_h and the mean thermocline depth might be due to that most wind stress momentum is trapped above the thermocline [*An and Bong*, 2016; *An and Kim*, 2017]. Here we compute the correlation between the intermodel mean thermocline depth averaged over the equatorial zonal band (5°S–5°N) and β_h , which is -0.2 (also see Figure S1 for the spatial correlation pattern with respect to β_h). The thermocline depth here is defined as 17° isotherm depth. As shown in above equation, β_h is also inversely proportional to g' , and g' is directly related to oceanic stability or simply the vertical density gradient. Thus, we compute the correlation coefficient between the intermodel β_h and the intermodel mean vertical temperature gradient ($\frac{\partial T}{\partial z}_{100\text{m}} - \frac{\partial T}{\partial z}_{250\text{m}}$) averaged over the equatorial band (5°S–5°N) for the whole Pacific basin. The resulting correlation coefficient is 0.37, which is statistically significant at the 90% confidence level, indicating that the relationship between β_h and g' is marginally significant.

In the previous paragraph, we explored the relationship between β_h and oceanic mean states, which showed a somewhat reasonable relationship but not one that was strongly significant. Here β_h was computed by using the zonal mean equatorial wind stress and the equatorial zonal contrast of thermocline depth anomalies between the eastern and western Pacific. By taking the zonal mean of wind stress, the effect of wind patterns could not be taken into account, while its effect is inherently imprinted in β_h . This is because apart from the wind intensity, the oceanic wave response depends on the horizontal wind stress pattern [*Im et al.*, 2015; *An and Kim*, 2017]. For example, changes in the zonal location of wind stress patches modify the oceanic wave response and oceanic adjustment time scales [*An and Wang*, 2000], and the meridional shape of wind stress influences them, too [e.g., *Kirtman*, 1997; *Chen et al.*, 2015; *Im et al.*, 2015; *McGregor et al.*, 2016]. Especially, the meridional shape of wind stress is related to the off-equatorial Rossby generation because it determines the intensity of wind stress curl, and then obviously, the reflection of such Rossby waves at the Pacific western boundary directly influences the equatorial western Pacific thermocline depth anomalies, so consequently β_h .

To measure such wind pattern's effects, especially its meridional shape, we compute the correlation coefficient between the intermodel sensitivity parameter (μ^*) and the intermodel β_h (Figure 3b). Here μ^* is the sensitivity of equatorially asymmetrical wind stress curl anomalies with respect to the eastern equatorial Pacific SSTA (Niño-3.4), which generates the off-equatorial Rossby waves. μ^* was computed from $\langle \nabla \times \vec{\tau} \rangle = \mu^* \langle T \rangle_{\text{Niño3.4}}$, where $\langle \nabla \times \vec{\tau} \rangle = 0.5 (\nabla \times \vec{\tau}_{\text{NH}} - \nabla \times \vec{\tau}_{\text{SH}})$ is an asymmetrical wind stress curl, and the subscripts NH and SH indicate the domain averages over 175°E–150°W and 2.5–7.5°N for

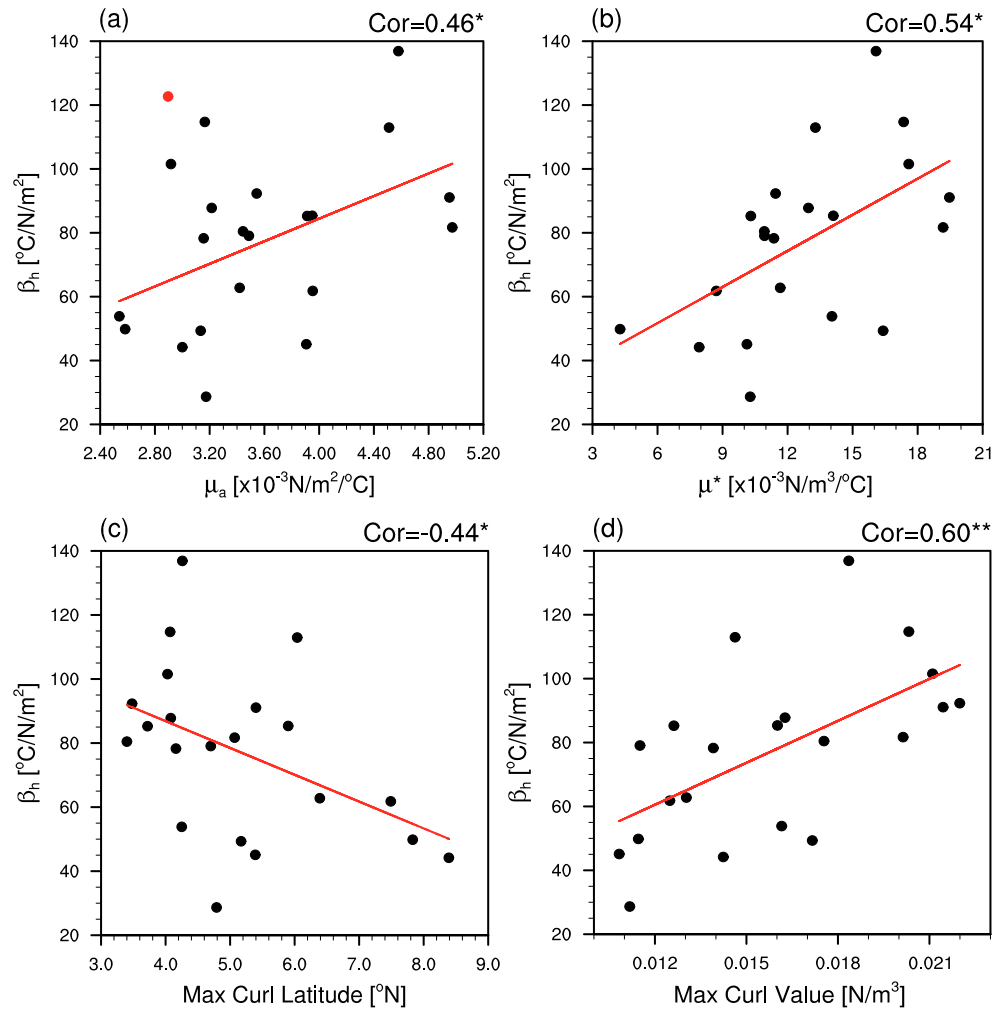


Figure 3. Scatterplots (a) between μ_a ($10^{-3} \text{ N m}^{-2} ^{\circ}\text{C}^{-1}$) and β_h ($^{\circ}\text{C N}^{-1} \text{ m}^{-2}$), (b) between μ^* ($10^{-3} \text{ Nm}^{-3} ^{\circ}\text{C}^{-1}$) and β_h ($^{\circ}\text{C N}^{-1} \text{ m}^{-2}$), (c) between the latitude of maximum wind stress curl ($^{\circ}\text{N}$) and β_h ($^{\circ}\text{C N}^{-1} \text{ m}^{-2}$), and (d) between the maximum wind stress curl (Nm^{-3}) and β_h ($^{\circ}\text{C N}^{-1} \text{ m}^{-2}$) obtained from CMIP5. Correlation coefficients are presented in the upper right corner of each panel, where single asterisk and double asterisk indicate a statistically significance at the 95% and 99% confidence levels, respectively. Red dot in Figure 3a is the observed-based one for comparison with the models.

Northern Hemisphere (NH) and 2.5–7.5 $^{\circ}\text{S}$ for Southern Hemisphere (SH). The resultant correlation is 0.54 ($p < 0.05$), which is slightly greater than the correlation between μ_a and β_h ($\rho = 0.46$; $p < 0.05$) (Figure 3a). Such rather small difference in a correlation may be due to a correlation between μ_a and μ^* ($\rho = 0.45$; $p < 0.05$). However, difference in a partial correlation becomes somewhat significant such that a partial correlation between β_h and μ^* with a third variable of μ_a is 0.42, while that between β_h and μ_a with a third variable of μ^* is 0.29. Equatorially asymmetrical wind stress curl is driven by the equatorially symmetrical zonal wind stress, and thus, a more equatorially confined zonal wind pattern leads to a stronger equatorially asymmetrical wind stress curl [An and Bong, 2016]. As we see from the correlations, the model-to-model differences in β_h are more closely related to those in μ^* than μ_a . This may be due to the higher efficiency of Rossby waves along the equatorial western Pacific thermocline change [e.g., McGregor et al., 2016].

We further check whether the comparatively high correlation between μ^* and β_h is due to the latitudinal location of the maximum wind stress curl or the intensity of the maximum wind stress curl. The former is determined by the meridional shape of the wind stress pattern, while the latter is related to both the

meridional shape and intensity of wind stress. In order to obtain the latitude and intensity of the maximum wind stress curl using each model simulation, we first computed a regression map of the tropical Pacific wind stress curl anomalies against the Niño-3.4 index from each model simulation and then identified the latitude and intensity from the regression map. As shown in Figure 3c, β_h is negatively correlated to the latitude of the maximum wind stress curl ($\rho = -0.44$; $p < 0.05$). This is because as the latitude of the maximum wind stress curl increases, Rossby waves are reflected less at the western boundary [Cane and Sarachik, 1977]. Actually, a higher correlation is found between the intermodel β_h and the intermodel maximum value of wind stress curl ($\rho = 0.60$; $p < 0.01$). Clearly, the strong wind stress curl corresponds to the larger β_h . We concluded that the intermodel diversity in the sensitivity of the intensity of the off-equatorial wind stress curl to ENSO-related SSTA is responsible for the intermodel diversity in the ENSO amplitude through modifying the ocean wave response.

4. Summary and Discussion

In this study, we investigate the origin of the intermodel diversity of ENSO variability among 21 CMIP5 models by computing SVD between the intermodel tropical Pacific SSTA variance and the intermodel BJ index. The first SVD mode explains 74% of intermodel SSTA variance, featuring an ENSO-like pattern, and 50.6% of the intermodel BJ index variance, which is dominated by TH. The model-to-model differences in TH are most significantly correlated to those in β_h and second to those in μ_a . The intermodel β_h is well correlated to the intermodel sensitivity of the off-equatorial wind stress curl intensity to ENSO-related SSTA. Therefore, the intermodel diversity of SSTA-to-surface wind stress curl response is primary responsible for the intermodel diversity in the ENSO amplitude through modification of the oceanic Rossby wave response.

The origin of the intermodel diversity in the intensity of wind stress curl might be complicated to determine. For example, the maximum value of the wind stress curl for a given equatorially symmetric bell-type zonal

wind stress ($\tau_x = \tau_M(0)e^{-\left(\frac{y}{L_y}\right)^2}$) is given by

$$(\nabla \times \tau_x)_{\max} = \pm \sqrt{\frac{2}{e}} \frac{\tau_M(0)}{L_y}, \quad (2)$$

where $\tau_M(0)$ is the zonal wind stress at the equator, where the maximum of zonal wind stress is assumed to be located, and L_y is the e -folding meridional scale (for the derivation of equation (2), see An and Bong [2016, Appendix 2]). Here we also assume that the meridional wind stress is negligible. As in equation (2), the maximum wind stress curl is proportional to the intensity of zonal wind stress at the equator, implying a significant relationship between μ_a and μ^* , and inversely proportional to the e -folding scale. Obviously, the intermodel μ^* and the intermodel maximum value of wind stress curl are well correlated, with a correlation coefficient of 0.77 ($p < 0.01$). On the other hand, the e -folding scale is defined as $L_y \approx \sqrt{\frac{2C_g}{\beta}}$

[Holton and Hakim, 2013], where C_g is the phase speed of a gravity wave that mainly is involving an atmospheric adjustment to a given forcing, and β is a meridional gradient of the Coriolis effect. Since the gravity wave speed is proportional to Brunt-Vaisala frequency [Battisti et al., 1999] or similarly the static stability (i.e., $\frac{1}{\theta} \frac{\partial \theta}{\partial z}$), a stably stratified atmosphere might have large e -folding scale and consequently a smaller maximum value of wind stress curl. The correlation map of the intermodel Brunt-Vaisala frequency near the surface boundary layer (925 hPa) against the intermodel μ^* shows statistically significant negative values over the tropical Pacific (see Figure S2). Therefore, as Brunt-Vaisala frequency is larger, the wind stress curl response to SSTA is weaker. On the other hand, the gravity speed is also proportional to the scale height, and so the larger Brunt-Vaisala frequency is corresponding to the higher scale height [An, 2011]. Since the steady state atmospheric response to a SST anomaly can be understood an adjustment within the atmospheric boundary layer in the tropics [Lindzen and Nigam, 1987; Battisti et al., 1999], the aforementioned scale height is presumably related to the height of atmospheric boundary layer. In other words, as the atmospheric boundary layer becomes deeper (i.e., corresponding to the larger Brunt-Vaisala frequency), the atmospheric response to the SSTA is expected to be weaker.

Acknowledgments

This research was supported by the Basic Science Research Program through the National Research Foundation of Korea (NRF) funded by the Ministry of Science, ICT and Future Planning (2014 R1A2A1A11049497). The authors appreciate all data providers, which can be found at the following web addresses: ERSSTv3b at <http://www.esrl.noaa.gov/psd/data/gridded/data.noaa.ersst.html>, SODA v2.2.4 at http://sodaserver.tamu.edu/assim/SODA_2.2.4/, and CMIP5 at <http://www.pcmdi.llnl.gov/>.

References

- An, S.-I. (2011), Atmospheric responses of Gill-type and Lindzen-Nigam models to global warming, *J. Clim.*, *24*, 6165–6173.
- An, S.-I., and H. Bong (2016), Inter-decadal change in El Niño–Southern Oscillation examined with Bjerknes stability index analysis, *Clim. Dyn.*, *47*, 967–979.
- An, S.-I., and I.-S. Kang (2001), Tropical Pacific basin-wide adjustment and oceanic waves, *Geophys. Res. Lett.*, *28*, 3975–3978, doi:10.1029/2001GL013363.
- An, S.-I., and J.-W. Kim (2017), Role of nonlinear ocean dynamic response to wind on the asymmetrical transition of El Niño and La Niña, *Geophys. Res. Lett.*, *44*, 393–400, doi:10.1002/2016GL071971.
- An, S.-I., and B. Wang (2000), Interdecadal change of the structure of the ENSO mode and its impact on the ENSO frequency, *J. Clim.*, *13*, 2044–2055.
- Battisti, D. S., E. S. Sarachik, and A. C. Hirst (1999), A consistent model for the large-scale steady surface atmospheric circulation in the tropics, *J. Clim.*, *12*, 2956–2965.
- Bellenger, H., E. Guilyardi, J. Leloup, M. Lengaigne, and J. Vialard (2014), ENSO representation in climate models: From CMIP3 to CMIP5, *Clim. Dyn.*, *42*, 1999–2018.
- Borlace, S., W. Cai, and A. Santos (2013), Multidecadal ENSO amplitude variability in a 1000-yr simulation of a coupled general climate model: Implications for observed ENSO variability, *J. Clim.*, *26*, 9399–9407.
- Cai, W., et al. (2015), ENSO and greenhouse warming, *Nat. Clim. Change*, *5*, 849–859.
- Cane, M. A., and E. S. Sarachik (1977), Forced baroclinic ocean motions. Part II: The linear bounded case, *J. Mar. Res.*, *35*, 395–432.
- Capotondi, A., et al. (2015), Understanding ENSO diversity, *Bull. Am. Meteorol. Soc.*, *96*, 921–938.
- Carton, J. A., and B. S. Giese (2008), A reanalysis of ocean climate using Simple Ocean Data Assimilation (SODA), *Mon. Weather Rev.*, *136*, 2999–3017.
- Chen, L., T. Li, and Y. Yu (2015), Causes of strengthening and weakening of ENSO amplitude under global warming in four CMIP5 models, *J. Clim.*, *28*, 3250–3274.
- Christensen, J. H., et al. (2013), Climate phenomena and their relevance for future regional climate change, in *Climate Change 2013: The Physical Science Basis. Contribution of Working Group I to the Fifth Assessment Report of the Intergovernmental Panel on Climate Change*, edited T. F. Stocker et al., pp. 1217–1308, Cambridge Univ. Press, Cambridge.
- Collins, M., et al. (2010), The impact of global warming on the tropical Pacific ocean and El Niño, *Nat. Geosci.*, *3*, 391–397.
- Guilyardi, E. (2006), El Niño–mean state–seasonal cycle interactions in a multi-model ensemble, *Clim. Dyn.*, *26*, 329–348.
- Ham, Y.-G., and J.-S. Kug (2015), Improvement of ENSO simulation based on intermodal diversity, *J. Clim.*, *28*, 998–1015.
- Hirst, A. C. (1986), Unstable and damped equatorial modes in simple coupled ocean–atmosphere models, *J. Atmos. Sci.*, *43*, 606–630.
- Holton, J. R., and G. J. Hakim (2013), *An Introduction to Dynamic Meteorology*, 5th ed., 552 pp., Academic Press, New York.
- Huang, B., V. F. Banzon, E. Freeman, J. Lawrimore, W. Liu, T. C. Peterson, T. M. Smith, P. W. Thorne, S. D. Woodruff, and H.-M. Zhang (2014), Extended Reconstructed Sea Surface Temperature version 4 (ERSST.v4): Part I. Upgrades and intercomparisons, *J. Clim.*, *28*, 911–930.
- Im, S.-H., S.-I. An, S. T. Kim, and F.-F. Jin (2015), Feedback processes responsible for El Niño–La Niña amplitude asymmetry, *Geophys. Res. Lett.*, *42*, 5556–5563, doi:10.1002/2015GL064853.
- Jin, E. K., et al. (2008), Current status of ENSO prediction skill in coupled ocean–atmosphere models, *Clim. Dyn.*, *31*, 647–664.
- Jin, F.-F., S. T. Kim, and L. Bejarano (2006), A coupled-stability index for ENSO, *Geophys. Res. Lett.*, *33*, L23708, doi:10.1029/2006GL027221.
- Kang, I.-S., S.-I. An, and F.-F. Jin (2001), A systematic approximation of the SST anomaly equation for ENSO, *J. Meteorol. Soc. Jpn.*, *79*, 1–10.
- Kim, S. T., and F.-F. Jin (2011), An ENSO stability analysis. Part II: Results from the twentieth and twenty-first century simulations of the CMIP3 models, *Clim. Dyn.*, *36*, 1609–1627.
- Kim, S. T., W. Cai, F.-F. Jin, A. Santos, L. Wu, E. Guilyardi, and S.-I. An (2014), Response of El Niño sea surface temperature variability to greenhouse warming, *Nat. Clim. Change*, *4*, 786–790.
- Kirtman, B. P. (1997), Oceanic Rossby wave dynamics and the ENSO period in a coupled model, *J. Clim.*, *10*, 1690–1704.
- Li, G., and S.-P. Xie (2012), Origins of tropical-wide SST biases in CMIP multi-model ensembles, *Geophys. Res. Lett.*, *39*, L22703, doi:10.1029/2012GL053777.
- Lin, J.-L. (2007), The double-ITCZ problem in IPCC AR4 coupled GCMs: Ocean–atmosphere feedback analysis, *J. Clim.*, *20*, 4497–4525.
- Lindzen, R. S., and S. Nigam (1987), On the role of sea surface temperature gradients in forcing low-level winds and convergence in the tropics, *J. Atmos. Sci.*, *44*, 2418–2436.
- Magnusson, L., M. Alonso-Balmaseda, and F. Molteni (2013), On the dependence of ENSO simulation on the coupled model mean state, *Clim. Dyn.*, *41*, 1509–1525.
- McGregor, S., A. Timmermann, F.-F. Jin, and W. S. Kessler (2016), Charging El Niño with off-equatorial westerly wind events, *Clim. Dyn.*, *47*, 1111–1125.
- McPhaden, M. J. (2003), El Niño and La Niña: Causes and global consequences, in *Encyclopedia of Global Environmental Change: The Earth System: Physical and Chemical Dimensions of Global Environmental Change*, 1, edited by M. C. MacCracken and J. S. Perry, pp. 355–370, Wiley, New York.
- Oueslati, B., and G. Bellon (2015), The double ITCZ bias in CMIP5 models: Interaction between SST, large-scale circulation and precipitation, *Clim. Dyn.*, *44*, 585–607.
- Taylor, K. E., R. J. Stouffer, and G. A. Meehl (2012), An overview of CMIP5 and the experiment design, *Bull. Am. Meteorol. Soc.*, *485*–498, doi:10.1175/BAMS-D-11-00094.1.
- Wallace, J. M., C. Smith, and C. S. Bretherton (1992), Singular value decomposition of wintertime sea surface temperature and 500-mb height anomalies, *J. Clim.*, *5*, 561–576.
- Xu, K., C.-Y. Tam, C. Zhu, B. Liu, and W. Wang (2017), CMIP5 projections of two types of El Niño and their related tropical precipitation in the twenty-first century, *J. Clim.*, *30*, 849–864.
- Yeh, S. W., J. S. Kug, and S. I. An (2014), Recent progress on two types of El Niño: Observations, dynamics, and future changes, *Asia-Pac. J. Atmos. Sci.*, *50*, 69–81.